Impact of light polarization on angle-resolved light scattering from gloss scale

I Gozhyk, Colette Turbil, E Garcia, G Obein

Impact of light polarization on angle-resolved light scattering from gloss scale.

I Gozhyk[1], C Turbil[1]‡, E Garcia[1]§ and G Obein[2]

[1] SVI, UMR 125 CNRS/Saint-Gobain Recherche, 39 quai Lucien Lefranc, 93303 Aubervilliers, France

[2] CNAM, Saint-Denis, France

iryna.gozhyk@saint-gobain.com

March 2023

Abstract. The gloss scale is a set of coated paper samples with different surface roughness allowing for appearance variation from high gloss to mat. Nowadays, the gloss scale is widely used as a reference on visual appearance of glossy and mat surfaces. This work provides for angle resolved analysis of light scattering from gloss scales as well as the analysis of the surface topography parameters relevant for the analysis of light-scattering experiments: RMS-roughness σ, auto-correlation function and power spectrum density, correlation length ℓ_c and surface slopes. The angle–resolved measurements of light scattered in reflection within the half–space are performed at 4 angles of incidence, while measurements within the incidence plane are made at 17 angles of incidence and under non–polarized, s– and p–polarized illumination. The polarization of incident light has a significant impact on both the specular and the diffused components of scattered light. Brewster scattering angle is especially well observed for black mat surfaces. Qualitative and quantitative analysis of measured scattered light is made with Rayleigh-Rice and Kirchhoff models applied to statistically representative analysis of surface topography.

1. Introduction

Light incident on an object of any size can be partially reflected or transmitted, diffusely scattered due to the surface roughness or the sub-surface inhomogeneities and partially absorbed. The visual appearance of the object depends strongly on the interplay between these phenomena as well as on the resulting angular distribution of scattered light. For instance, the glossy appearance is related to the amount of light reflected along the direction of specular reflection, i.e. along the direction predicted by Snell-Descartes law. Major pioneering works on light scattering were done by no one else but Lord Rayleigh first in 1871 on sub-wavelength particles and then in 1895 and 1907 on periodically

‡ Present address: to fill

§ Present address: to fill

corrugated reflection grating [1]. This latter work, known as vector-perturbation theory for light scattering from rough surfaces, represents the scattered field as an infinite sum of plane waves. The surface needs to be rather smooth for solution to converge, it is valid for moderate scattering angles but otherwise the theory is valid for both non-conductive and conductive samples [1]. Based on more recent interpretations from Rice in 1951 [1, 2], the theory is often referred to as Rayleigh-Rice vector perturbation theory. Meanwhile, physical optics allows for a different approach for phenomenological description of light scattering from rough surfaces: light diffraction caused by random phase variations in reflected wavefront from surface topography. It is precisely the meaning of Kirchhoff approximation introduced in 1952 by Brekhovskikh [2] but commonly known in the form published in the notorious book by Beckmann and Spizzichino [3] and therefore referred to as Beckmann-Kirchhoff model. Unlike Rayleigh-Rice theory, Beckmann-Kirchhoff model can address not only optical quality but rough surfaces, yet it is more restrictive in surface statistics (see Appendix 5 for details), and valid for moderate angles of incidence and non-conductive surfaces. Interesting improvements for this model were suggested by J. Harvey [2], but they are computationally more demanding than original expressions.

In spite of more than a century long advancements in physical optics on the analysis of light scattering from the rough surfaces and light scattering from volume inhomogeneities, it remains impossible to analytically address a complex case of rough surfaces with sub-surface inclusions of arbitrary size and concentration. Moreover, in what concerns the light scattering from rough surface the analytic descriptions exist for very smooth surfaces (Rayleigh-Rice theory) or rather rough surfaces (Beckmann-Kirchhoff model) [1]. Meanwhile, optical properties of *arbitrary* rough surface with roughness comparable to the wavelength of the incident light can only be correctly addressed with numerical simulations based on resolution of Maxwell equations. Such calculations have to be done for several realizations of surface topography with common statistical properties, at all the wavelength and angles of incidence of interest etc. From the computational point of view this task is extremely demanding. Therefore, the physical optics mainly focuses on the link between the surface topography and its optical properties for rather smooth surfaces, which can be addressed with approximated methods (Rayleigh-Rice theory, reduced Rayleigh equations [4] etc.).

The parametric description of the half-space distribution of light scattered by surfaces of different nature [5] is necessary to produce virtual reality images. Due to above described tremendous complexity of this problem from the optical point of view, since about 1990s the computer graphics community was investing substantial efforts into the experimental study of angular distribution of light intensity scattered from real-life objects [6]. The goal was to explore the link between the angular distribution of light scattered by the object and its appearance. Such angle-resolved measurements were performed on large panel of materials including automotive, spray and house paints, gems, wood, plastics, metals, ceramics, fabrics and human skin; and are accessible through databases such as Cornell [7], MERL from Disney [8], NIST, CERRET from Columbia-

Ultrecht, RGL from EPFL and others.
Such empiric approach has allowed for a great evolution in computer graphics. Yet, its utility for physically-realistic rendering as well as for the field of light scattering is limited by two obstacles. First, the vast majority of the angle-resolved data on light scattering available online are devoted to samples with unique appearance, while rather scarce information is given on the sample structure (surface topography, concentration of subsurface inclusions etc.). Naturally, quite a few modern surfaces can be identified as 'white plastics', yet their optical properties and appearance might differ significantly. For the appearance classification to be reproducible and predictable, the angle-resolved analysis must be done either on samples with known topography [9, 10] and subsurface structure, or on standard or reference samples [11] for which the sample structure is known and samples are freely accessible. Secondly, not all such measurements contain information on the state of polarization of the incident light used to obtain them. Yet, both specular [12] and scattered [13, 14] components of reflection and transmission can exhibit polarization-dependent features. And in fact physically–realistic appearance can only be achieved if such effects are taken into account.
Despite the rich information the angle–resolved measurements can bring in, the setups providing for such measurements are still rare within both academic and industrial communities due to their high cost and the time investment such measurements require. In fact, measurements of integral properties related to light scattering, such as reflectance, diffuse reflection, gloss and haze etc., remain the key tools used in the academia and on the production lines. It is thereby very important to study the impact of the angular distribution of the scattered light on its integral properties.

In summary, study of the impact of surface topography on its optical properties is one of the core activities of physical optics. This approach requires a detailed knowledge of surface topography and can be computationally very demanding, which limits its application to real-life surfaces. In the mean time, during last decades there was a tremendous progress in measurement of the angle-resolved optical properties of real life rough surfaces and understanding how they impact the object appearance. But to the very large extend, the surface topography is not regarded in such studies. In this paper an alternative approach to the problem is proposed. We focus on the set of samples produced by the same fabrication process and having different appearance, known as the gloss scale. These samples are accessible to very large community and are already widely used as a visual reference for surfaces with glossy and mat appearance, for example for visual quality check or as a reference for design. This work provides an extensive experimental study of the surface topography of these samples as well as their angle-resolved and integral optical properties. The textbook optical models such as Rayleigh and Kirchhoff are used for the analysis of different features of angle-resolved scattering distributions under non-polarized, s- and p-polarized illumination.

The paper is organized as follows. First, section 2 samples studied in this work are described, including the analysis of their topography and integral optical properties

such as gloss and specular and diffused reflectivity spectra. The angle-resolved optical properties under non-polarized illumination are described within section 3, while the polarization-induced effects on specular and scattered light are shown and discussed in section 4. If the reader is not familiar with basic notions on light scattering from rough surfaces, such as statistical estimators of surface topography relevant for light scattering problem, definitions on reflectivity, gloss and angle-resolved scattering and theoretical models for their prediction, it is recommended to start with Appendix 5 which provides the basic notions on these phenomena.

2. Description of the samples

This study focuses on the gloss scale samples commercialized by NCS, which are widely used in the industry and in the metrology related to gloss. NCS gloss scale samples are made of opaque paper, covered with mixture of pigments and porous varnish. This section presents the samples examined in this work, their surface topography and integral optical properties.

NCS gloss scale contains 28 samples representing 7 levels of gloss from 2 to 95 GU in 4 colors each: white, light gray, dark gray and black. Figure 1 shows the optical photographs of full gloss (a) and full mat (b) samples at grazing angles of incidence.

Figure 1. NCS gloss scale samples: optical photographs of (a) full gloss and (b) full mat NCS samples, 2 GU and 95 GU gloss respectively, taken in the photo booth with D65 illumination; (c) measured vs nominal gloss. In (a,b) samples are black, dark gray, clear gray and white from left to right correspondingly.

Nominal gloss values of NCS gloss scale are calculated with respect to ISO 2813 standard [15] at 60°: full mat (2 GU), mat (6 GU), semi-mat (12 GU), satin (30 GU), semi-glossy (50 GU), glossy (75 GU) and full gloss (95 GU). Figure 1.(c) provides a comparison of nominal gloss and gloss measured white NCS samples with glossmeter device Pico Glossemaster Model 500 commercialized by Enrichsen. This apparatus

measures gloss in reflection at 20° and 60° angles of incidence. Note that for samples with <10 GU (i.e. full mat and mat samples) additional measurement at 85° is recommended, but the authors did not have means to perform it at a time of study.

Figure 2 provides the optical microscopy photographs of the sample surface for black (top) and white (bottom) samples of different GU values. As is witnessed by Figure 2, the decrease of the gloss level (from right to left) is achieved by the increase of the amount and size of diffusers and absorbers in the coatings. Moreover, the coatings seem to be macro-porous in full mat, mat and semi-mat samples.

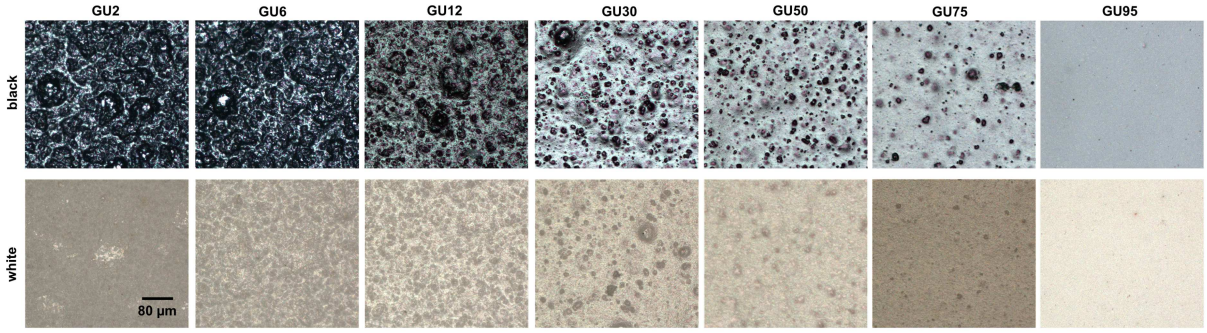

Figure 2. Optical microscopy photographs of NCS black (top line) and white (bottom line) samples with gloss varying from 2 GU(left) to 95 GU (right).

The surface topography was measured by the stylus profilometer (Dektak XT, Bruker) with the tip diameter $D = 2\ \mu m$. Obtained 1D surface profiles $h(x)$, i.e. the interface between the sample and the ambient medium, were defined in such a way that the sample was below the profile, i.e. at $z < h(x)$. The scan length was $L = 6\ mm$, which resulted from measurement at $N = 12001$ points with equidistant measurement step Δ=0.5μm. Albeit rather large scan length and number of measurement points, at least 5 profiles per sample were measured to guarantee statistically-representative analysis [16, 17]. Results of the statistical analysis of surface topography, including deduced parameters of mounded surfaces (see Appendix 5 for details), is given in Table 1. Figure 3 shows autocorrelation function (a), Power Spectrum Density (b) and standard deviation of slope distribution (c) for samples with different gloss. These figures, as well as related statistical estimators gathered in Table 1, show that the mat surfaces (GU2, GU6 and GU12) exhibit different statistics compared to semi-glossy (GU30 and GU50) and glossy surfaces (GU75 and GU95). Auto-correlation functions (Figure 3(a)) of the mat surfaces (GU2, GU6 and GU12) show a rapid decay at small values of shift which we speculate to be related to the surface microstructure induced by the coating porosity. Power Spectrum Density functions normalized by $\pi\sigma^2\ell_c^2$ (Figure 3(b)) exhibit a pic at $q_x = \frac{2\pi}{\Lambda}$ for semi-glossy (GU30 and GU50) and glossy surfaces (GU75 and GU95). Finally, the standard deviation of slope distribution depicted on Figure 3(c) is different for examined samples and strongly scale-dependent. The RMS roughness

and other characteristic length are shown in Figure 4(a) and Table 1. Interestingly, the RMS roughness as well as ℓ_c, Λ do not exhibit constant decay or augmentation with the sample gloss. However, σ/ℓ_c decays with gloss as shown by Figure 4(b). In summary, the analysis of surface topography based on roughness only allows to discern the full mat (2 GU) and mat (6 GU) samples from others. In order to properly recognize all samples from the set it is necessary to analyze the in-plane correlations. Moreover, these samples are excellent candidates for a thorough comparison of gloss and the angle-resolved light scattering.

Sample (GU)	σ (μm)	ℓ_c (μm)	Λ (mm)	α (arb. units)	ℓ_0/Λ (arb. units)
2	1.57	32	0.8	0.7	0.25
6	1.22	27.5	1.6	0.26	0.25
12	0.73	24.1	0.6	0.39	0.24
30	0.75	110	2.9	0.11	0.04
50	0.56	130	2.0	0.31	0.09
75	0.45	340	2.0	0.18	0.85
95	0.42	370	2.3	0.70	0.74

Table 1. Statistical estimators of surface topography of examined white NCS samples. RMS roughness (σ) and correlation length ℓ_c deduced from measured 1D height profiles. Parameters Λ, ℓ_0 and α describing the ACF of mounded surface as deduced from fit of ACFs with eq.10.

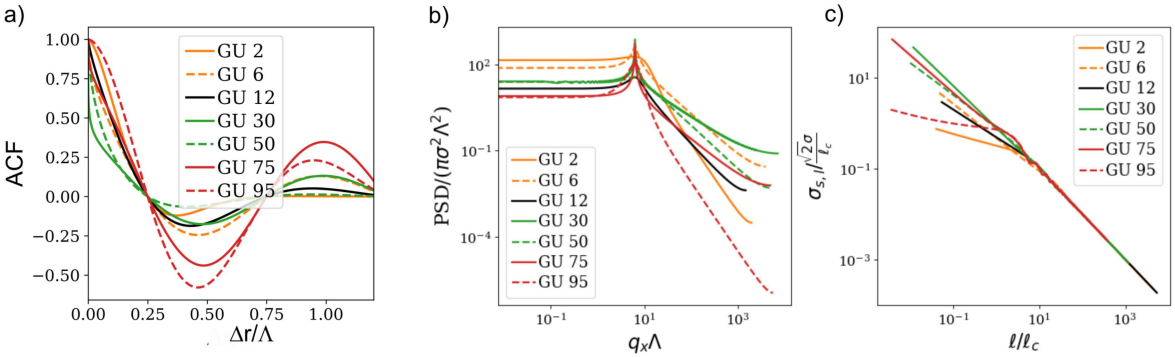

Figure 3. Statistical estimators of surface topography of white NCS samples: (a) ACF, (b) PSD and (c) standard deviation of slope distribution. For the sake of comparison the axes are rendered dimensionless. (b) represents a 2D PSD plotted for $q_y = 0$. These PSDs were obtained with eq.3,4 from the fit of experimental ACFs (see Table1). Here $\sigma_s^* = \frac{\sigma\sqrt{2}}{\ell_c}$.

Optical reflectance spectra were obtained with Lambda 950 spectrometer commercialized by Perkin Elmer. Reflectance measurements R^h were performed with

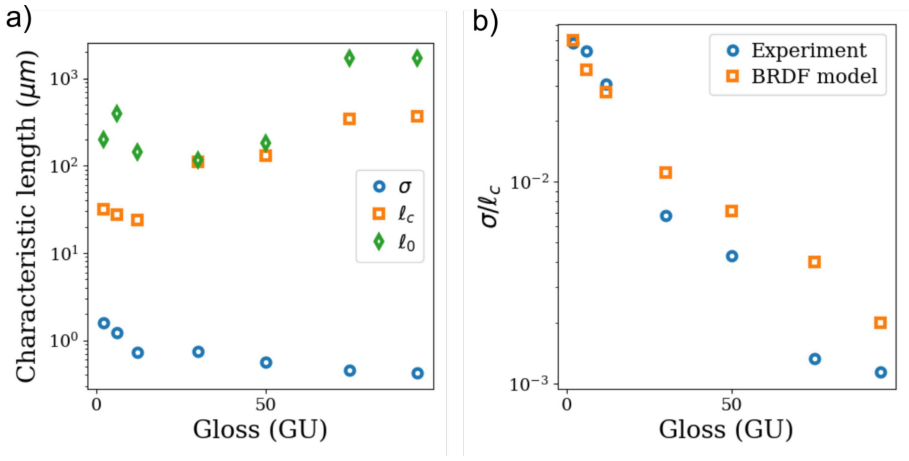

Figure 4. Statistics on the topography of NCS samples (a) characteristic length and (b) σ/ℓ_c obtained from surface topography measurements on white NCS samples and from the analysis with Kirchhoff model of the angle-resolved BRDF averaged over 4 shades of NCS samples.

non-polarized illumination (within the visible spectral range) at the θ_i=8° and with the integrating sphere, while during the measurements of diffused reflectance R^{sc} the cone of 4° around the specular direction was left out from the integrated sphere. Finally, R was deduced from these two measurements following eq.16. Figure 5(a) depicts the specular and diffused reflection from white NCS samples of different gloss at 589 nm. The measured specular reflectivity follows a linear rise with gloss, at the exception of low reflectivity points where the measured value is comparable with measurement uncertainty. Based on 17, one can link the reflectivity of the measured and reference sample $R = Gloss \cdot R_{ref}$. Yet the reference sample is not perfectly flat, meaning that it's reflectivity R_{ref} is actually smaller than $R_{0,ref}$ the reflectivity of the perfectly flat surface made of the same material as the reference sample. In fact, $R_{0,ref}$ = can be deduced from eq.13-14 with n=1.51 (see Appendix 5 for details). Interestingly, we find an empiric relation $R = 0.7Gloss \cdot R_{0,ref}$ for examined samples. This empiric relation is depicted by dashed olive line on Figure 5(a).

As shown by Figure 5(a) for white samples, the diffused reflection can be assumed constant with gloss. Figure 5(b) shows diffused reflectivity of gloss samples of different color and their deduced Lambertian BRDF. If one assumes that all the diffused reflection is Lambertian, the f_r^L component of BRDF can be estimated from eq.(18) (see Appendix 5 for details), as shown on Figure 5(b), and is of about $2.7.10^{-1}sr^{-1}$ for white, $1.6.10^{-1}sr^{-1}$ for clear gray, $8.3.10^{-2}sr^{-1}$ for dark gray and $1.4.10^{-2}sr^{-1}$ for black sample. In what follows these values will be used for comparison with magnitudes of diffused components obtained through the angle-resolved measurements.

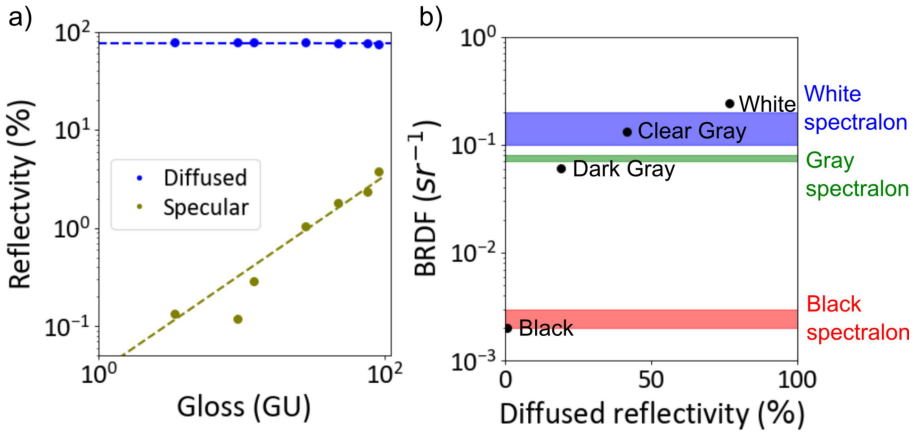

Figure 5. (a) measured specular and diffused reflection vs measured gloss for white samples, (b) deduced Lambertian-like BRDF for samples of different shades. Specular reflection R at 8° obtained with the illumination wavelength of 589 nm of all white NCS samples. Blue dashed line depicts the average diffused reflectivity of NCS white samples of different shades, while olive dashed line depicts empiric relation $R = 0.7{\cdot}Gloss{\cdot}R_{0,ref}$ as described in the paper. (b) The Lambertian BRDF is deduced from diffused reflectivity with eq.20. For the sake of comparison, colored regions depict Lambertian BRDF values reported [1] for black (red color), gray (blue color) and white (blue color) spectralon samples.

3. Impact of the surface roughness on the angle-resolved light scattering

This section is devoted to the angle-resolved analysis of light scattering in reflection from NCS samples under non-polarized illumination. It is of the common knowledge, that in the case of the small surface roughness, typically described in the literature through the ratio of RMS roughness and the illumination wavelength $\sigma << \lambda$ [1,18], the angle-resolved intensity of scattered light contains two main features: the specular spike and the comparatively broad lobe, centered at the direction of the specular reflection. In the case of large surface roughness, $\sigma \propto \lambda$ [3], specular spike is not observed anymore, while the lobe centered around specular direction becomes even broader. Finally, in the case of very rough surfaces, $\sigma > \lambda$, due to the masking and shadowing of surface elements, at non-normal incidence the center of this lobe shifts towards the angles of scattering larger than the one of specular reflection [19,20]. Although examined samples have RMS roughness comparable or larger compared to the illumination wavelength (as shown in Table1), they exhibit all three above-described BRDF types. In this section, the general features of measured BRDF such as Lambertian-like background scattering and the forward scattering lobe are discussed.

This section starts with the description of the setup used in this work and its different measurement configurations. Then it focuses on the general overview on the

angle-resolved scattering of all NCS gloss scale samples. The specular BRDF at different angles of incidence is analyzed with Kirchhoff BRDF model, while the angular distributions are analyzed with Rayleigh-Rice BRDF model.

3.1. Measurement setup

Angle-resolved measurements of optical intensity in far field were made with OMS4 goniospectrophotometer commercialized by OPTIS, schematically shown in Fig. 6(a) and described in details elsewhere [21]. Due to the sample opacity, only angle-resolved optical intensity scattered in reflection was measured. If not explicitly mentioned otherwise, the incident light source was incoherent Xenon lamp light filtered around the center wavelength $\lambda = 535$ nm by a window of width 10 nm. This light source is non-polarized, yet in some experiments presented in this work linear polarizers were used resulting in s- and p-polarized illumination. In the measurements performed in this study the dimension of luminous spot on the sample was 8 mm, beam divergence was 0.17°, and thereby the maximum measurable BRDF [1] was 4300 sr^{-1}.

Angle-resolved intensity of reflected light was collected either within the plane of incidence, referred hereafter as in-plane scan, or within the half-space. All the reflected light, independent of polarization, was detected. The half-space measurements were performed with non-equidistant angular sampling, with a minimum measurement step of 0.5° around the specular direction and maximum step of 2.5° far from the specular direction. Such measurements were performed at 4 polar angles of incidence $\theta_i = 15°$, 30°, 45° and 60°. The contour plots of the half-space BRDF, as the one shown on the polar plot on Fig. 6(b) for NCS white 12 GU sample illuminated at $(\theta_i, \phi_i) = (30°, 180°)$, were plotted with the home-made python code. Such representation allows one to grasp all the features of the scattering diagram in the whole half space, for instance specular peak and diffused lobes. The specular direction of reflection in Fig. 6(b), and in the experimental results to be presented, is at $(\theta_r, \phi_r) = (\theta_i, \phi_i - 180°) = (\theta_i, 0°)$. The black color on Fig. 6(b) represents the angular regions where no measurements were performed. In particular, the region in the vicinity of $\phi_r = 270°$ and $\theta_r >= 60°$ is inaccessible to the detector (due to the physical dimensions of the support on which the setup is mounted), while in the region around $\phi_r = 180°$ and $\theta_r = \theta_i$ the detector arm covers for the source.

Slightly different notations are used for in-plane measurements: $\theta_r \in [0°, 90°)$ for the forward scattering (i.e. $\phi_r = 0°$), while $\theta_r \in (-90°, 0°]$ for backward scattering (i.e. $\phi_r = 180°$).The in-plane measurements were performed with a measurement step 0.5°. Measurements were performed at 17 polar angles of incidence $\theta_i = 0°$, 4°, 6° and [10°, 75°] with 5° step. Fig. 6(c) compares the in-plane BRDF distributions measured at several θ_i. Such plots allow for quantitative comparison between different samples and illumination conditions.

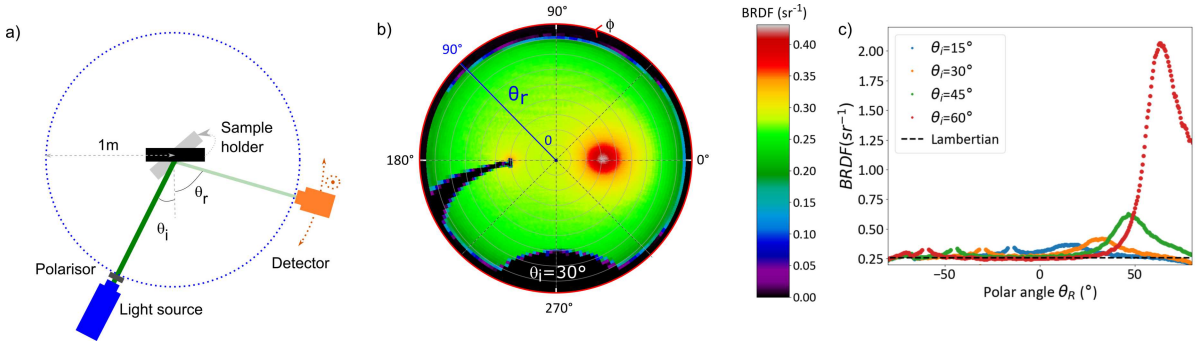

Figure 6. Scheme of OMS4 goniospectrophotometer (a) and angular distribution of the BRDF measured with it of NCS white semi-mat (12 GU) sample illuminated with non-polarized light: (b) the full half-space distribution of BRDF for θ_i= 30°; (c) the BRDF within the incidence plane measured at θ_i= 15°, 30°, 45° and 60°. In (c) all the reflected light, independent of polarization, was detected. The Lambertian scattering component with BRDF=0.26sr^{-1} shown in black dash line was calculated from R^{sc} measurement with eq.20.

Angular distributions of the BRDF plotted in Figure 6 for white semi-mat (12 GU) sample present 3 distinguished features: i) the Lambertian-like scattering with $f_r\left(\theta_i, \theta_R, \phi_R\right) = const$ (precisely 0.26 sr^{-1}), ii) forward-scattering lobe centered at $(\theta_r, \phi_r) = (\theta_i, 0°)$ and iii) back-scattering lobe centered at $(\theta_r, \phi_r) = (\theta_i, 180°)$ with its central part being in the non-measurable area (the source obscured by detector arm). Note that Fig. 6 shows no specular spike, which is expected to be the case for a semi-mat sample.

In order to analyze how each of these features varies with θ_i, the average of 5 measurements within the plane of incidence are compared for different samples or measurement conditions, as depicted on Fig. 6b. In what follows there is no analysis of back-scattering lobe, since the data are incomplete due to the fact that the source is obscured by the detector arm.

3.2. Angle-resolved scattering for all NCS samples

Now we will more closely inspect the intensities and positions of the three lobes (diffuse, specular and back-scattering) on the example of NCS samples with different GU. Figure 7 depicts BRDF measured within the plane of incidence at $\theta_i = 20°, 45°, 60°$ and 75° (columns from the left to the right respectively) of all NCS white, clear gray, dark gray and black samples and GU values from 2 to 95 (rows from the top to the bottom respectively).

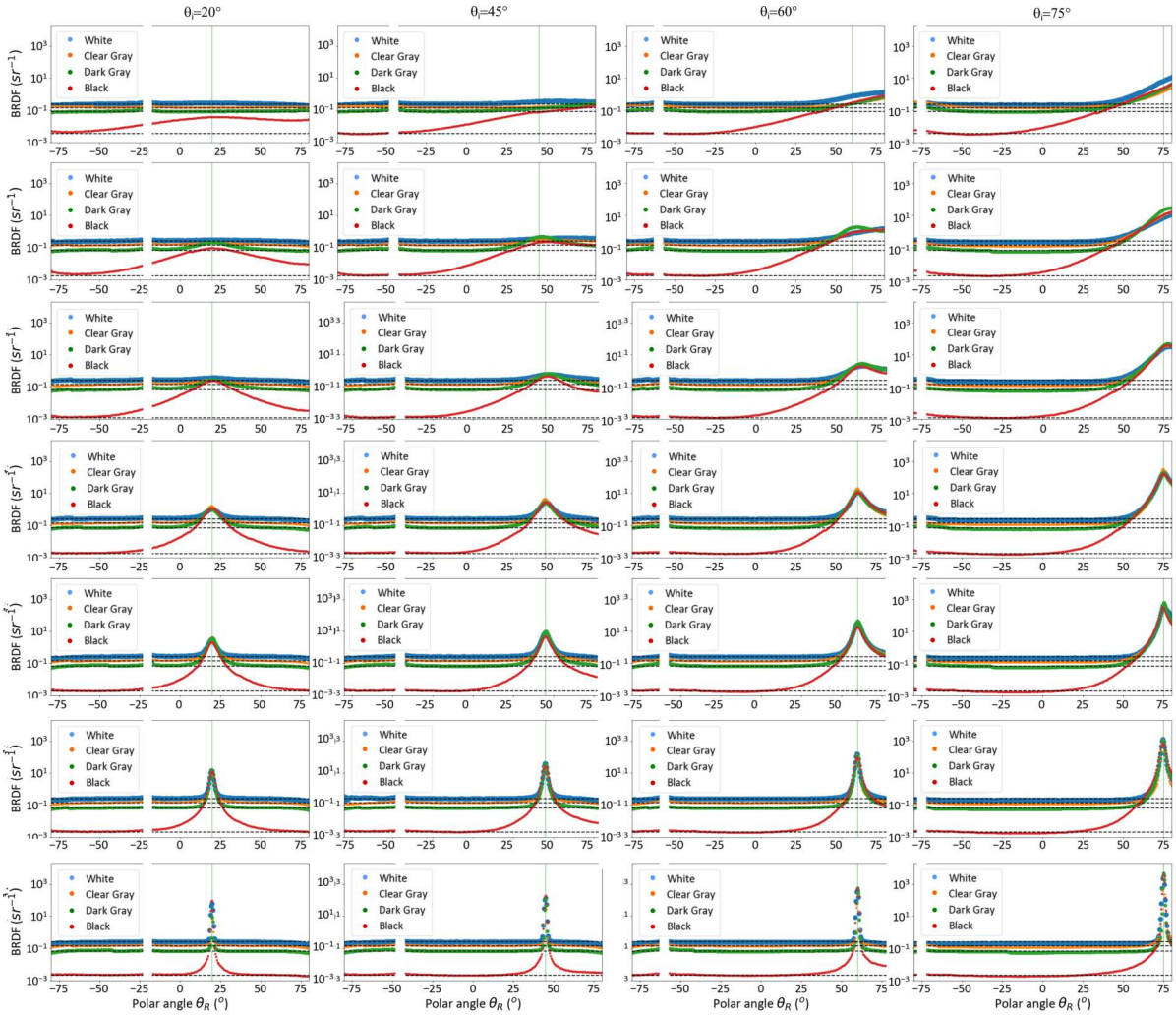

Figure 7. BRDF in the plane of incidence of NCS white, clear gray, dark gray and black samples at $\theta_i = 20°$ (first column from the left), 45° (second column), 60° (third column) and 75° (forth column). Each line corresponds to samples of the same GU. Lambertian components are shown in dash line for each sample and are independent of θ_i. The absence of data in vicinity of $\theta_R = -\theta_i$ is related to the fact that the source is obscured by detector in this area.

3.2.1. Lambertian-like component All plots on Figure 7 contain a flat Lambertian-like component f_r^L, which for painted paper is known to originate from light scattering in the material below the surface [1]. The magnitude of f_r^L can be read at a flat part of BRDF curve for θ_r in range $[-30°, 0°]$ at θ_i=45° and 60°, as in the definition of contrast gloss [22–24]. In fact, f_r^L depends on the amount and size of diffusers and absorbers in the paint, and thereby varies with sample shade but is independent on the GU as witnessed by Figures 7 and 8(a). Based on the angle-resolved measurements depicted in Figure 7, f_r^L is about $2.6.10^{-1} sr^{-1}$ for white, $1.5.10^{-1} sr^{-1}$ for clear gray, $7.8.10^{-2} sr^{-1}$ for dark gray and $7.7.10^{-3} sr^{-1}$ for black samples. For non-black samples these values are in good agreement with theoretical values of f_r^L deduced from the diffused reflectivity

measurements in section 2. The experimental f_r^L value for black sample lays within the range $[5.5 - 8.0]10^{-3}sr^{-1}$ reported for black spectralon [1]. Yet, the value deduced from the diffused reflectivity measurements is about 2 times higher. The overestimation of the BRDF of diffused lobe from diffused reflectivity measurement is caused by the assumption, that all the light scattered outside the specular peak contributes to the Lambertian scattering. But in black samples the subsurface scattering is so low, that the integral over the broad forward scattering lobe represents about a half of all scattered light.

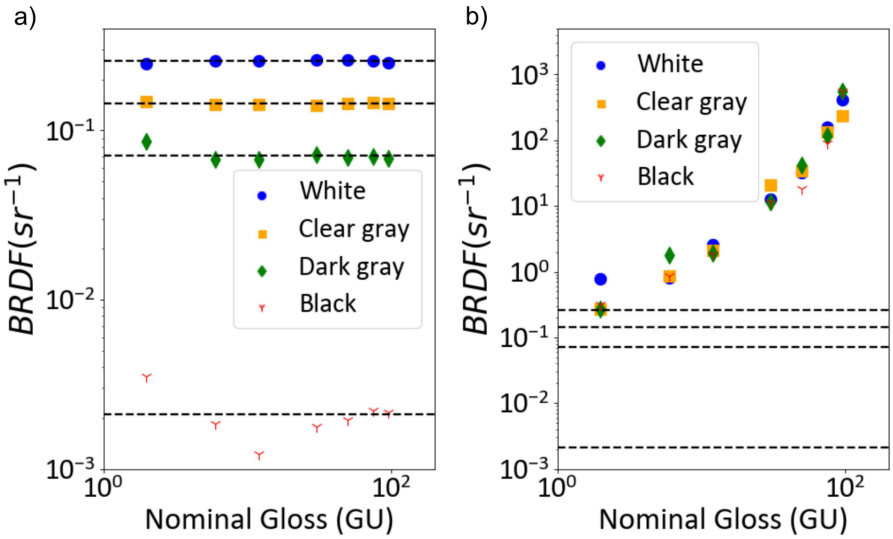

Figure 8. BRDF features under non-polarized illumination. (a) Lambertian-like BRDF and (b) specular BRDF at $\theta_i = 60°$ for all NCS samples.

3.2.2. Forward scattering BRDF values at specular reflection for illumination at $\theta_i = 60°$ are depicted on Fig. 8(b) for all samples. Samples of different shades do not have exactly the same BRDF, but nevertheless measured values are in good agreement with previously reported ones for painted paper: 200 sr^{-1}, 30 sr^{-1} and 2.5 sr^{-1} for high, medium gloss and mat samples respectively [1]. Figure 8(b) also shows rather satisfactory comparison of measured specular reflection components and those predicted from Kirchhoff model.

As shown by Figure 7, the forward scattering lobe is clearly distinguishable in the data for black samples regardless the θ_i or GU. At the incidence angles $\theta_i \geq 45°$ the forward scattering lobe becomes asymmetric with respect to the specular reflection direction. For 12 GU and higher gloss samples the forward scattering lobe is centered around the direction of specular reflection. In samples with lower GU the forward scattering lobe is seen for samples of all colors at large θ_i only, while the maximum of this lobe happens at angles larger than the angle of specular reflection. For 75 GU and

higher the specular spike is observed. Note that if surface roughness is evaluated as a ratio of RMS to wavelength, then according to Table1 our examined samples exhibit rather large and very large roughness, meaning no specular spike should be observed for any of these samples. Meanwhile, as shown by Table 2, the ratio of RMS roughness to correlation length in examined surfaces seems to be a better indicator of surface roughness. As will be shown in next section, the angular distribution of BRDF for small GU is shaped by the difference in BRDF under s- and p-polarized illumination.

Sample	σ/ℓ_c	σ/ℓ_c^*
	Surface topography	Kirchhoff model
2 GU	49.10^{-3}	12.10^{-2}
6 GU	44.10^{-3}	36.10^{-3}
12 GU	30.10^{-3}	28.10^{-3}
30 GU	68.10^{-4}	11.10^{-3}
50 GU	43.10^{-4}	71.10^{-4}
75 GU	13.10^{-4}	69.10^{-4}
95 GU	11.10^{-4}	24.10^{-4}

Table 2. σ/ℓ_c as obtained from surface topography of white gloss samples and from the analysis with Kirchhoff model eq.25 (see Appendix 5 for details) of the specular BRDF as averaged over 4 sample colors. ℓ_c^* indicates the assumption of Gaussian ACF.

4. Impact of the polarization of incident light

This section focuses on the angle-resolved scattering of all NCS gloss scale samples under *s*- or *p*-polarized illumination. The impact of light polarization on specular BRDF at different angles of incidence is analyzed with Kirchhoff BRDF model. The BRDF within the whole hemisphere under p-polarized illumination is analyzed with Rayleigh-Rice BRDF model.

Figure 9 has a similar structure compared to Figure 7, but depicts BRDF of all NCS white and black samples measured within the plane of incidence under s- and p-polarized illumination. Figure 9 shows that polarization of incident light impacts not only the amplitude of the specular component but also the diffused component of light scattered by sample surface.

Figure 10 summarizes how the main features of Figure 9, namely the amplitude of BRDF at specular reflection direction (Fig. 10(a)-(b)) and θ_B^{sc} (Fig. 10(c), see Appendix 5 for details), vary with the sample gloss (Fig. 10(a)) or the angle of incidence (Fig. 10(b)-(c)). The surface-induced component of BRDF can be distinguished only in the case when measured BRDF at a given incidence and scattering angle is larger as compared to the Lambertian-like component related to the sub-surface scattering. At 60° incidence specular components of BRDF under s-polarized illumination are larger than their

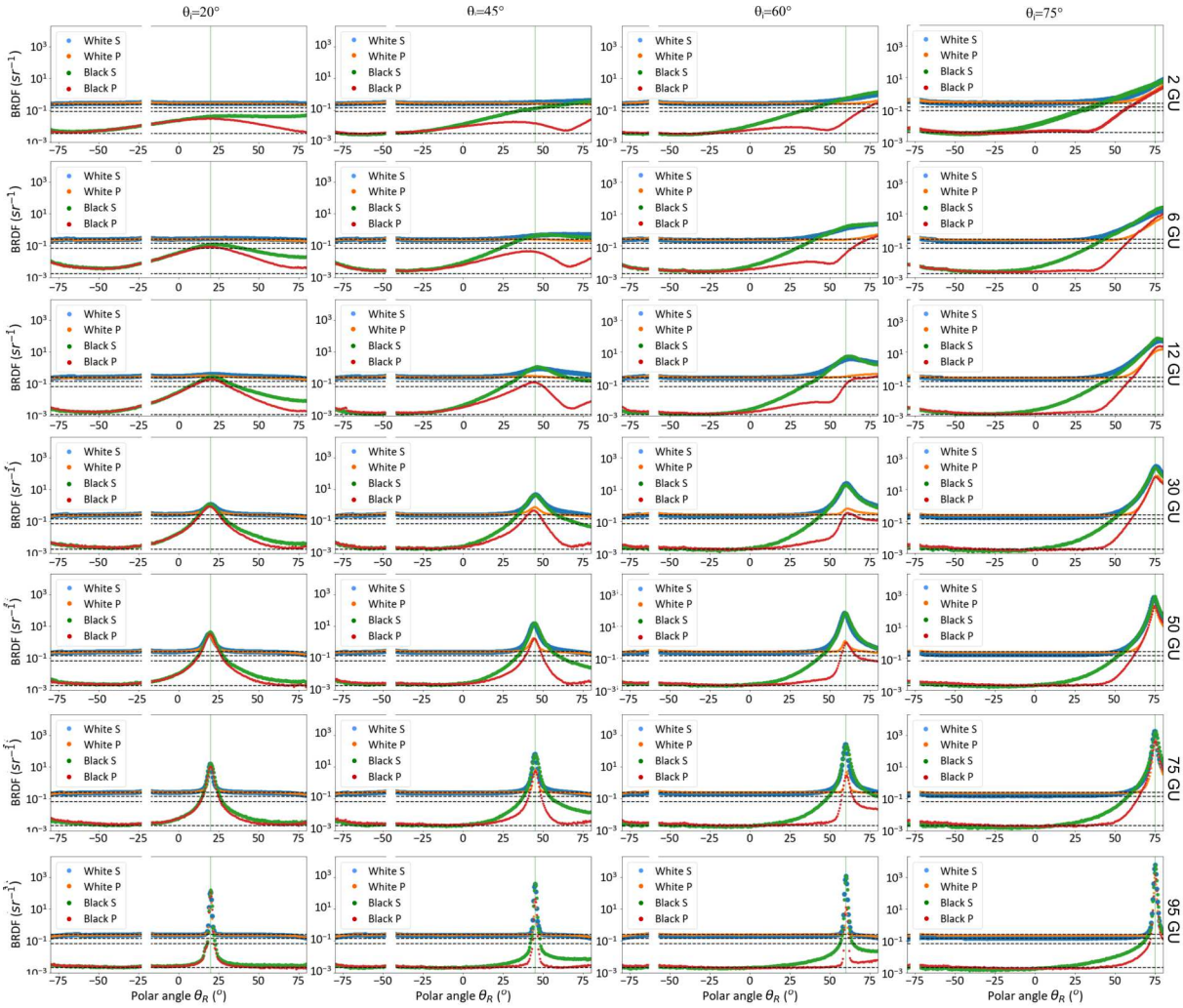

Figure 9. BRDF in the plane of incidence of NCS white and black samples at $\theta_i = 20°$ (first column from the left), 45° (second column), 60° (third column) and 75° (forth column) obtained with s- or p-polarized illumination. Each line corresponds to samples of the same GU. Lambertian components as measured with non-polarized illumination are shown in dash line for comparison for white, clear gray, dark gray and black sample.The absence of data in vicinity of $\theta_R = -\theta_i$ is related to the fact that the source is obscured by detector in this area.

Lambertian counterpart for samples of all GU and all shades. As shown by Fig. 10(b), the Kirchhoff model allows to reproduce rather well the angle-resolved variation of specular component under s-polarized illumination. The surface topography values σ/ℓ_c deduced from such angle-resolved analysis for samples with different GU are summarized in Figure 4(b) and Table 2. The BRDF values predicted for such surfaces with Kirchhoff model at specular direction under s-polarized and p-polarized illumination at $\theta_i = 60°$ are superposed with experimental data on Figure 9(a).

Let us now focus on light scattered by sample surface away from specular direction and the analysis of Brewster scattering angle in examined samples. Indeed, in Figure

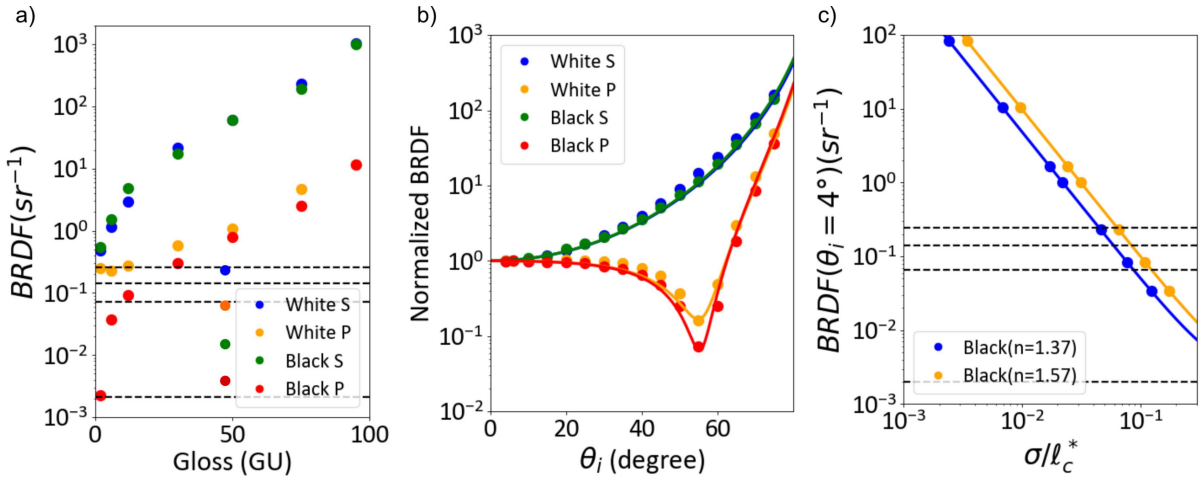

Figure 10. Main features of BRDF curves shown on Fig. 9: (a) BRDF at specular reflection direction at $\theta_i = 60°$ for black and white samples of different GU; (b) BRDF at specular reflection direction of GU 95 white and black samples under s- and p-polarized illumination as a function of the angle of incidence; (c) specular BRDF component at small incidence ($\theta_i = 4°$) calculated from eq.26 while varying σ/ℓ_c for surface with refractive index n=1.37 (blue curve) and n=1.57 (yellow curve). Data points represent measured specular BRDFs on black samples (under assumption that n=1.37 or n=1.57). Solid lines in (b) depict the estimations based on Kirchhoff model (eq.25) with n=1.51 (GU95).

9 a clear dip is seen at $\theta_i = 45°$ and 60° under p-polarized illumination in all black samples of gloss $\leq$ 30 GU. In white and gray samples this effect is not observed since the subsurface scattering is larger than the surface-induced scattering under p-polarized illumination. Fig. 10(c) shows Brewster scattering angles for black 2 and 6 GU samples and at different angles of incidence.

Figure 11 shows the full half-space angular distributions of BRDF measured (a-c) and calculated Q_p factor. Bright spots seen on Figure 11.(a-c) at $\phi \in (40°; 60°)$ and $\phi \in (90°; 130°)$ are parasitic reflections related to the linear polarizor introduced into the illumination bench. Note that there is a small sample tilt which will be impossible to see if not for half-space measurements.

The minima of the half-space distributions of experimental BRDF Figure 11.(a-c) and the calculated Q_p factors shown in Figure 11.(d-f) do not perfectly coincide. The comparison of measured BRDF and calculated BRDF and accounting for the sample tilt might provide for a more precise result. Yet our primary intention was to show that based on measurements at several AOI and without complex calculations the refractive index can be identified rather well.

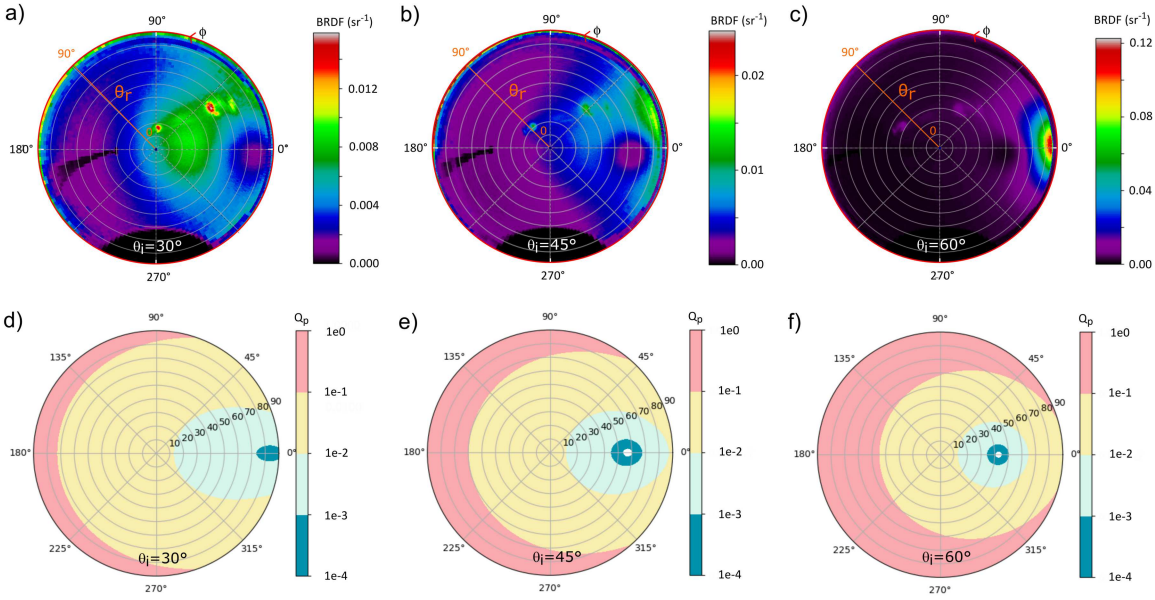

Figure 11. Full half-space angular distribution of (a-c) measured BRDF of NCS black mat (2 GU) sample and (d-f) calculated Q_p factor. Incident illumination was p-polarized, while the angle of incidence was (a,d) θ_i= 30°, (b,e) θ_i= 45° and (c,f) θ_i= 60°. In (a-c) the source of the incident light was a Xenon lamp filtered around the center wavelength λ = 535nm by a window of width 10 nm. All the reflected light, independent of polarization, was detected. Figures (d-f) were calculated for material with refractive index n=1.37 as deduced from Figure10(c).

5. Conclusions

This work is dedicated to thorough experimental study of surface topography and angle-resolved light-scattering of a set of gloss samples as well as their qualitative analysis based on classic physical optics models, such as Rayleigh-Rice and Kirchhoff models. Examined samples are made of opaque paper with a pigment-containing coating on a top of it, and are widely used for visual assessment of gloss. This set of samples provides for a rare opportunity to study angle-resolved optical scattering from samples with different appearance and obtained with the same fabrication process.

Thorough analysis of surface topography reveals rather large surface roughness (RMS roughness varying from $0.4\mu m$ to $1.6\mu m$ for white NCS samples) in mat and glossy samples. This suggests that surface roughness can not be correctly evaluated based on RMS roughness alone. In examined samples the RMS roughness decays with sample GU, while correlation length ℓ_c increases with sample GU. The ratio σ/ℓ_c decays from about 5.10^{-2} (in low gloss samples) to about $1.5.10^{-3}$ (in high gloss samples). In the case of mounded surfaces, to which examined samples belong, the auto-correlation function exhibits a complex oscillating behavior which can not be described by a single

ℓ_c parameter. Nevertheless the ratio σ/ℓ_c, used for the analysis of light scattering from rough surfaces in Kirchhoff model, can be used for qualitative assessment of the impact of surface roughness on gloss. It is of a common practice in BRDF community to describe surface topography through the distribution of surface slopes. It is however a scale-dependent parameter, and thereby particular attention should be put to the scale at which it is estimated. Yet, the local slopes at the scale of ℓ_c are relatively small even for samples with lowest gloss.

Angle-resolved light scattering of these gloss samples exhibit Lambertian-like component, related to subsurface scattering, and a surface induced scattering component, the angular width of which decreases with sample gloss. The Lambertian-like component does not depend on the angle of incidence and the sample gloss, but on the sample shade. It is about $2.6.10^{-1}sr^{-1}$ for white, $1.5.10^{-1}sr^{-1}$ for clear gray, $7.8.10^{-2}sr^{-1}$ for dark gray and $7.7.10^{-3}sr^{-1}$ for black NCS samples. These values are comparable with previously reported for spectralon samples [1]. Angle-resolved scattering related to surface scattering is much more complex, since it varies with the angle of incidence, the sample gloss and also the polarization of incident light. In order to perform a meaningful analysis of all experimentally-obtained data, including surface topography and optical scattering data, two different physical optics models, Rayleigh-Rice and Kirchhoff models, were used to analyze the surface-induced light scattering.

Kirchhoff model, as described by Beckmann and Spizzichino [1,3], was deduced for surfaces with Gaussian auto-correlation function. Yet, it provides rather good prediction of the specular component of BRDF based on the known ratio σ/ℓ_c and refractive index, as well as the variation of this specular component with the angle of incidence. The Rayleigh-Rice model provides for relevant information regarding the normalized angle-resolved scattering. In particular, it allows for prediction of Brewster scattering angle based on the refractive index of sample surface. In the case when subsurface scattering is low compared to surface scattering under p-polarized illumination, such angle-resolved measurements at several angles of incidence can be actually used for the identification of the refractive index of the surface.

In summary, NCS gloss samples exhibit polarization-sensitive BRDF properties: Fresnel-like variation of specular component with clear Brewster angle under p-polarized illumination in high gloss samples, but also Brewster scattering angle in mat samples with small sub-surface scattering. The combination of Kirchhoff and Rayleigh-Rice models for light scattering from rough surfaces allows for both qualitative and quantitative analysis of the BRDF of glossy and mat samples.

Acknowledgments We thank Simon Mazoyer, Ingve Simonsen, Damien Vandembroucq and Sebastien Noygues for valuable discussions.

C.T. benefited from a PhD grant funded by Saint-Gobain Research Paris and

"Association Nationale de la Recherche et de la Technologie". This work was supported by French National Research Agency through FRAXOS project (ANR-15-CHIN-0003).This work has been done in the frame of the project 18SIB03 BxDiff, that has received funding from the EMPIR programme co-financed by the Participating States and from the European Unions Horizon 2020 research and innovation programme.

Appendix: Light scattering from rough surfaces

In this work we focus on the light scattering in reflection upon the illumination from a rough surface of height profile $h(\vec{r})$, with the ambient medium, air, being above the surface, i.e. $z > h(\vec{r})$, and scattering pigments present below the surface.

This section starts with the description of statistical estimators of surface topography used in different optical models on light scattering from rough surfaces. Then integral and angle-resolved optical properties of light scattering objects are introduced, including the description of two optical physics models on angle-resolved light scattering from rough surfaces.

5.1. Surface topography

Let us briefly discuss several statistical estimators of the surface topography of randomly rough surfaces (see [16] for details), relevant for light-scattering experiments, namely RMS roughness, lateral correlations and slopes.

In what follows we consider a height profile $h(\vec{r})$. This profile is assumed to be a single-valued function of $\vec{r} = (x, y)$ and differential with respect to both x and y. The height profile is also assumed to be a stationary, ergodic and zero-mean random process. The probability distribution function of the height values of this randomly rough surface is assumed to be Gaussian [16].

In such a case the vertical fluctuations of surface height are described by the root-mean-square (RMS) height, also referred to as the height standard deviation σ:

$$\sigma = \langle h^2(\vec{r})\rangle^{1/2}; \tag{1}$$

The spatial organization of surface roughness can be deduced from the surface height auto-covariance $\mathcal{I}(\Delta\vec{r})$:

$$\mathcal{I}(\Delta\vec{r}) = \langle h(\vec{r} + \Delta\vec{r})h(\vec{r})\rangle; \tag{2}$$

and its normalized version, the auto-correlation function (ACF) $\mathcal{A}(\Delta\vec{r})$:

$$\mathcal{A}(\Delta\vec{r}) = \frac{1}{\sigma^2}\mathcal{I}(\Delta\vec{r}). \tag{3}$$

The power spectrum density (PSD) function $\widetilde{\mathcal{I}}(\vec{q})$ is a counterpart of the auto-covariance in the Fourier space:

$$\widetilde{\mathcal{I}}(\vec{q}) = \int d^2r\mathcal{I}(\vec{r}) \exp\left(-i\vec{q}\cdot\vec{r}\right). \tag{4}$$

where $\vec{q} = (q_x, q_y)$ is the wave vector parallel to the mean surface. Note that in case of isotropic surfaces both ACFs and PSDs can be calculated from 1D profiles. However,

the normalisation of PSD differs in case of 1D scan since the integral of the PSD equals the variance of the height distribution σ^2 (Parseval's theorem [3, 16]).

Finally, in the case of a surface with Gaussian distribution of heights, the distribution of local slopes s_ℓ over the length-scale ℓ is also Gaussian:

$$p(s_\ell) = \frac{1}{\sigma_{s,\ell}\sqrt{\pi}} \exp\left(-\frac{s_\ell^2}{2\sigma_{s,\ell}^2}\right), \tag{5}$$

while the standard deviation of local slopes $\sigma_{s,\ell}$ can be estimated based on the surface ACF [16]:

$$\sigma_{s,\ell} = \frac{\sigma\sqrt{2}}{\ell}\sqrt{1-\mathcal{A}(\ell)}. \tag{6}$$

In this work we focus on three functional forms of ACF: the exponential, the Gaussian, and the ACF of mounded surfaces. In theoretical models, due to mathematical convenience, the preference is given to the Gaussian ACF:

$$\mathcal{A}(\Delta r) = \exp\left[-\left(\frac{\Delta r}{\ell_c}\right)^2\right], \tag{7}$$

and in some cases to exponential ACF:

$$\mathcal{A}(\Delta r) = \exp\left[-\frac{|\Delta r|}{\ell_c}\right]. \tag{8}$$

Here a correlation length ℓ_c is an estimate of the lateral length scale above which correlation is significant. Its conventional definition was developed for exponential and Gaussian ACFs:

$$\mathcal{A}(\ell_c) = 1/e. \tag{9}$$

In the fabricated real-life rough surfaces several characteristic length scales can coexist, representing the material micro-structure and the signature of the forming process. For example, the ACF of mounded surfaces exhibit a decay over length-scale ℓ_0 with an oscillatory behavior of length-scale Λ [18, 25]:

$$\mathcal{A}(\Delta r) = \exp\left[-\left(\frac{\Delta r}{\ell_0}\right)^{2\alpha}\right]\cos\left(\frac{2\pi\Delta r}{\Lambda}\right), \tag{10}$$

where α stands for the roughness exponent ($0 \leq \alpha \leq 1$). Figure 12.(a) illustrates these three functional forms of ACF, namely exponential, Gaussian and the ACF of mounded surface with $\alpha = 0.75$, $\Lambda = \ell_0$ and $\Lambda = 2\ell_0$. It is clear from Figure 12.(a) that the correlation length is linked in a complex way to the parameters ℓ_0, Λ and α of mounded surface. Meanwhile, the period Λ of mounded surface can be easily determined from the first zero crossover of ACF: $A\left(\frac{\Lambda}{4}\right) = 0$. $\sigma_s^* = \frac{\sigma\sqrt{2}}{\ell_c}$

The 2D-PSD of surface with Gaussian ACF is as follows:

$$\widetilde{\mathcal{I}}_{2D}(\vec{q}) = \pi\sigma^2\ell_c^2 \exp\left(-\left(\frac{q\ell_c}{2}\right)^2\right), \tag{11}$$

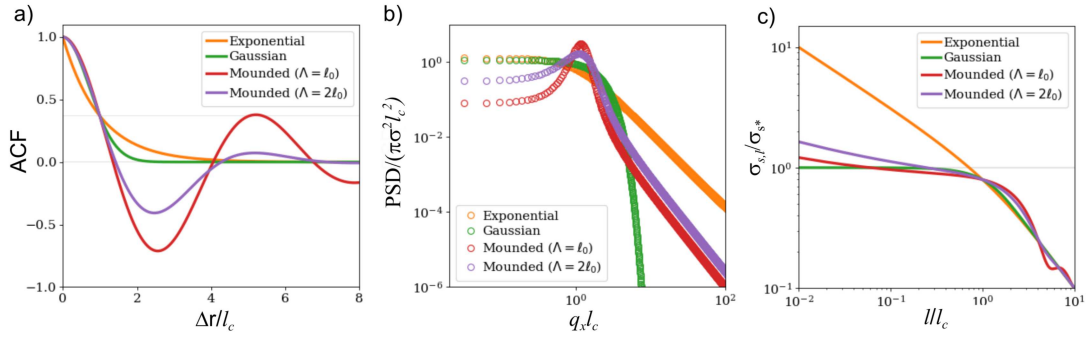

Figure 12. ACF (a), PSD (b) and standard deviation of surface slopes (c) of surfaces with exponential ACF, Gaussian ACF and mounded surfaces with $\alpha = 0.75$, $\Lambda = \ell_0$ ($\ell_c/\ell_0 = 0.19$) and $\Lambda = 2\ell_0$ ($\ell_c/\ell_0 = 0.35$). For the sake of comparison the axes are rendered dimensionless. (b) represents a 2D PSD plotted for $q_y = 0$.

while the 2D-PSD of surface with exponential ACF is:

$$\widetilde{\mathcal{I}}_{2D}(\vec{q}) = \frac{\pi\sigma^2\ell_c^2}{\left(1+(q\ell_c)^2\right)^{3/2}}. \tag{12}$$

Note that at q=0 $\widetilde{\mathcal{I}}(\vec{q}=0) = \pi\sigma^2\ell_c^2$ for surfaces with both Gaussian and exponential ACF (see low frequency tail for exponential and Gaussian ACF on Figure 12.(b)). Unfortunately, there is no analytical expression for PSD of mounded surfaces with an arbitrary α and it must be calculated from known ACF as a Fourier transform of auto-covariance function (eq.2,4). For the sake of illustration, Figure 12.(b) plots the PSDs of all the ACFs from Figure 12.(a). In mounded surfaces $\widetilde{\mathcal{I}}(\vec{q}=0)$ is not equal to $\pi\sigma^2\ell_c^2$ (low frequency tail of the PSD of the mounded surfaces on Figure 12.(b) differs from the one for the surfaces with exponential or Gaussian ACF).

Figure 12.(c) shows how the functional form of ACF impacts the slope distribution. In the case of Gaussian ACF, if ℓ is sufficiently smaller than ℓ_c the statistics of local slopes is independent of the length-scale ℓ over which the slopes are defined [16]. Probably for this reason the notion of the length-scale over which the slopes are calculated is absent in geometrical optics models, which were developed for surfaces with Gaussian ACF.

Yet this is no longer true in the case of surfaces with exponential ACF. Even more, for such surfaces at $\ell < \ell_c/2$ the mean surface slope decays drastically with ℓ. In mounded surfaces depending on the value of the roughness exponent α and ratio Λ/ℓ_0, slope statistics may exhibit rather *strong dependence on the length scale ℓ over which the slopes are defined* [16]. For instance, as depicted by Figure 12.(c) the standard deviation of the distribution of slopes in mounded surface with $\Lambda = \ell_0$ (red curve) exhibits non-monotonous decay with ℓ. This implies, that in order to be meaningful, the analysis of local slopes must be based on the statistics of the rough surface (RMS

roughness and ACF).
As will be shown below, the physical optics models account for surface roughness at different scales and thereby are capable to predict some features of the optical properties of real-life surfaces based on the surface topography. In contrast, the geometrical optics models rely on the distribution of slopes at a single length scale. This means that geometrical optics models may be useful for the deduction of the information on surface topography at a scale relevant for experimental conditions, based on the experimental optical data. They are however likely to fail in solving the direct problem: the prediction of the optical properties based on surface statistics.

5.2. Integral optical properties

This section focuses on the reflectivity, hemispherical reflection and gloss, while the angle-resolved optical properties are addressed in the next section. Throughout a paper the polar angle of incident illumination is θ_i, while the azimuthal angle of incidence is set to $\phi_i = 180°$. The polar and azimuthal angles of scattered light are (θ_r, ϕ_r) respectively, and the specular direction of reflection corresponds to $(\theta_r, \phi_r) = (\theta_i, 0°)$ with $\theta_r \in [0°, 90°)$ and $\phi_r \in [0°, 360°)$.

The *reflectivity*, i.e. the fraction of incident flux reflected along the specular direction, varies with the polar angle of incidence θ_i. For a perfectly flat surface the reflectivity coefficients R_s and R_p for s- and p-polarized incident light respectively are described by Fresnel coefficients, which for material with refractive index n and with air as the ambient medium reduce to:

$$R_{s,p}(\theta_i) = \left| \frac{a_{s,p}\cos\theta_i - \sqrt{n^2 - \sin^2\theta_i}}{a_{s,p}\cos\theta_i + \sqrt{n^2 - \sin^2\theta_i}} \right|^2, \tag{13}$$

where $a_s = 1$ and $a_p = n^2$. The reflectivity upon non-polarized illumination is:

$$R = \frac{R_s + R_p}{2}. \tag{14}$$

Figure 13(a) illustrates how R_s, R_p and R would vary with the θ_i in the case of reflection from a perfectly flat surface of black glass (n=1.567 [22]), silicon nitride (n=2.046 [26]) and gold (n=0.273 [27]) in air illuminated with monochromatic light source of a wavelength 589.3 nm. This allows to compare the metallic and dielectric surfaces, as well as understand the impact of the refractive index of dielectric material on reflectivity and BRDF. The Brewster angle, i.e. the θ_i, at which the reflectivity of p-polarized light equals zero, is given by expression:

$$\tan\theta_B = n. \tag{15}$$

In glass and polymers θ_B is about 56°, while the increase of refractive index with respect to the one of glass results in the decay of θ_B (see Figure13(a)).

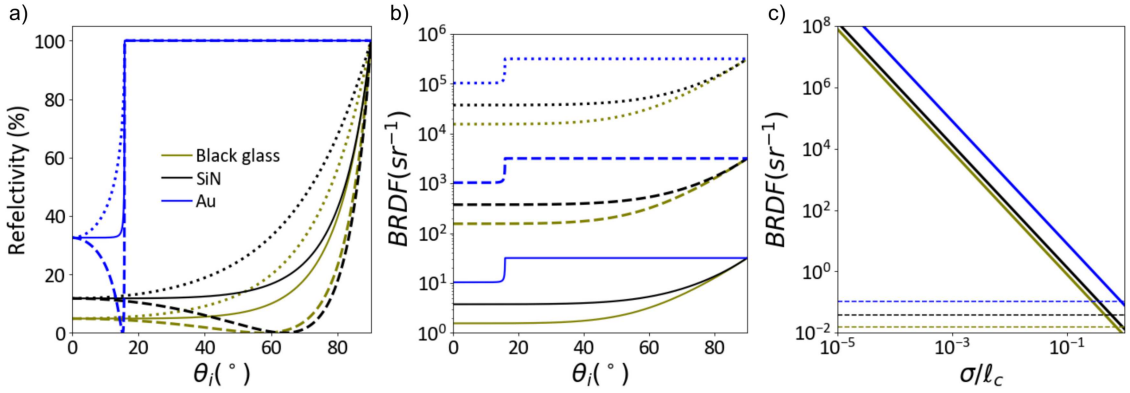

Figure 13. Impact of the refractive index surface material on its reflectivity (a) and specular BRDF of rough surface (b,c). (a) Reflectivity coefficients of s- (dotted line) and p-polarized (dashed line) and non-polarized (solid line) monochromatic incident light (@589.3 nm) as a function of θ_i calculated with eq.13-14 for perfectly flat surfaces made of different materials as described below. (b) Specular BRDF under non-polarized illumination as modeled by Kirchhoff model eq.25 for rough surface with Gaussian ACF with $\sigma/\ell_c = 0.001$ (dotted line), $\sigma/\ell_c = 0.01$ (dashed line) and $\sigma/\ell_c = 0.1$ (solid line).(c) Specular BRDF under non-polarized illumination incident at 60° as modeled by Kirchhoff model eq.25 for rough surface with Gaussian ACF and varied σ/ℓ_c. Horizontal dashed lines correspond to the Lambertian BRDF deduced from eq.20. Surface materials are black glass (green line, n=1.567 [22]), silicon nitride (gray line, n=2.046 [26]) and gold (blue line, n=0.273 [27]).

Even at a small surface roughness the fraction R^{sc} of the incident flux is inevitably scattered away from the specular direction at the expense of the specular component R. The hemispherical reflectance R^h is defined as follows:

$$R^h = R + R^{sc}, \tag{16}$$

The gloss is aimed to represent the flux of light scattered around the direction of specular reflection. The most common technique for experimental evaluation of gloss is the *specular gloss measurement*, done by integration of light intensity scattered in the close vicinity of specular direction. Such measurement is generally done with glossmeter device and the gloss value in gloss units (GU) is obtained. In the most commonly used configuration of glossmeter the gloss is defined as the total flux scattered inside a small angular region around the specular direction, normalized by the flux that is scattered by a standard reference sample, typically black glass with refractive index n=1.567 at 589.3 nm [22]; this ratio defines the "gloss unit" (GU) scale:

$$Gloss(\theta_i) = \frac{\int P(\theta_i)d\theta_i}{\int P_{ref}(\theta_i)d\theta_i} * 100(GU), \tag{17}$$

where P and P_{ref} are light flux values reflected from the sample and from the standard reference sample respectively and integrated within a solid angle of measurement around the specular direction. Specular gloss is at first measured at $\theta_i = 60°$. In the case of

high gloss samples,i.e. >60 GU, additional measurement is necessary at $\theta_i = 20°$. And in the case of low gloss samples, i.e. <10 GU, additional measurement is necessary at 85° [15, 22].

5.3. Angular distribution of light scattered in reflection

The bi-directional reflectance distribution function, BRDF or $f_r(\theta_i, \phi_i, \theta_r, \phi_r)$, is the main parameter used in experimentalists community to describe the angular distribution of scattered light. The BRDF is defined as a ratio of radiance of the surface to its irradiance and is the experimentally accessible quantity:

$$f_r(\theta_i, \phi_i, \theta_r, \phi_r) = \frac{P_s/\Omega_r}{P_i \cos\theta_r}, \tag{18}$$

where P_i stands for incident flux and P_s for flux scattered along the solid angle $\Omega_r = (\theta_r, \phi_r)$.

Meanwhile, the hemispherical reflectance R^h can be defined through the cosine-corrected BRDF, namely $f_r(\theta_i, \phi_i, \theta_r, \phi_r)\cos\theta_r$, also known as angle-resolved scatter, ARS, or differential scattering coefficient, DSC [1]:

$$R^h_m(\theta_i) = \int_0^{\pi/2}\int_0^{2\pi} f_{r,m}(\theta_i, \phi_i, \theta_r, \phi_r)\cos\theta_r \sin\theta_r d\theta_r d\phi_r, \tag{19}$$

where index $m = s, p$ indicates the polarization of the incident light.

If the object scatters light equally in all directions, so-called Lambertian diffuser, the link between the BRDF and reflectance is straightforward:

$$f_r^L(\theta_i, \phi_i, \theta_r, \phi_r) = \frac{R^h(\theta_i)}{\pi}. \tag{20}$$

Yet, wide-angle scattering is generally a signature of the sub-surface scattering rather than the signature of surface roughness.

There are several analytical approximated models for light scattering from rough surfaces (see for instance [1–3, 28]). We will focus on two oldest and widely known models which provide for rather simple analytic expressions linking surface topography and angle-resolved light scattering: the Rayleigh-Rice vector perturbation theory for smooth surfaces and Kirchhoff tangent model for rough surfaces.

The most commonly used form of Kirchhoff BRDF model was derived by Beckmann and Spizzichino [1,3] and accounts for the reflectivity coefficient $R(\theta_i)$ (see eq.(13-14)), for the masking-shadowing factor F and for the surface topography:

$$f_r(\theta_i, \phi_i, \theta_r, \phi_r) = \pi R(\theta_i) F^2(\theta_i, \phi_i, \theta_r, \phi_r) \left(\frac{L}{\lambda}\right)^2 e^{-\left(\frac{qL}{2}\right)^2}. \tag{21}$$

They define the masking-shadowing factor F as follows:

$$F(\theta_i, \theta_r, \phi_r) = \frac{1 + \cos\theta_i \cos\theta_r - \sin\theta_i \sin\theta_r \cos(\phi_r + \pi - \phi_i)}{\cos\theta_i (\cos\theta_i + \cos\theta_r)}; \tag{22}$$

while the topography and illumination conditions are defined jointly by the factor L and spatial frequency q:

$$L = \frac{\ell_c \lambda}{2\pi\sigma\left(\cos\theta_i + \cos\theta_r\right)}, \tag{23}$$

$$q = 2\pi \frac{\left[\left(\sin\theta_r \cos\phi_r - \sin\theta_i\right)^2 + \sin^2\theta_r \sin^2\phi_r\right]^{\frac{1}{2}}}{\lambda}. \tag{24}$$

This model was developed for surface with Gaussian ACF and therefore can not properly predict the angular distribution of light scattered from surface with other functional forms of ACF. However the specular reflection is defined by low-frequency region of PSD, which is generally constant with frequency (see Figure 12.(b)). This model can be useful for the analysis of the magnitude of BRDF at specular direction of reflection ($\phi_r = 0$, $\theta_r = \theta_i - \pi$):

$$f_r(\theta_i, \pi, \theta_i, 0) = \pi R(\theta_i) \left(\frac{\ell_c}{4\pi\sigma\cos\theta_i}\right)^2. \tag{25}$$

Figure 13(b) shows the angular distribution of the BRDF at the direction of specular reflection given by eq.25 for three different materials. It is clear that the angular distribution of the BRDF follows the same trend with the angle of incidence as the reflectivity, depicted in Figure13(a). Meanwhile, as illustrated in Figure13(c), the increase of the surface slopes results in the decay of BRDF, as one would logically expect. This figure also shows that when $\sigma > \ell_c/10$ the BRDF at specular direction approaches the value of the Lambertian BRDF of such surface. Finally, according to Kirchhoff BRDF model at small angles of incidence f_r simplifies to a following expression:

$$f_r\left(\theta_i \to 0, 0, \theta_i \to 0, 0\right) = \pi R\left(0\right) \left(\frac{\ell_c}{4\pi\sigma}\right)^2, \tag{26}$$

which can be useful for quick assessment the experimental studies of rough surfaces.

In the Rayleigh-Rice model, the surface roughness is considered to be a small perturbation of flat surface. The model is often said to be limited to the case of small surface roughness. However some authors suggest that Rayleigh-Rice model can describe surfaces with small surface slopes, i.e. to some extent small σ/ℓ_c [3]. According to the Rayleigh-Rice model the BRDF is proportional to 2D PSD of examined surface and to the reflectivity polarization factor Q:

$$f_r\left(\theta_i, \phi_i, \theta_r, \phi_r\right) = \frac{16\pi^2}{\lambda^4} \cos\theta_i \cos\theta_r Q I\left(\frac{q_x}{2\pi}, \frac{q_x}{2\pi}\right). \tag{27}$$

In the case of non-polarized source and polarization insensitive detector Q is as follows:

$$Q = \frac{1}{2} \sum_{\beta} \sum_{\gamma} Q_{\beta\gamma}, \tag{28}$$

where β and γ in $Q_{\beta\gamma}$ stand for polarization (s, p) of incident or scattered light respectively [1]. In the case of β state of incident polarization and polarization insensitive detector Q_β is:

$$Q_\beta = \sum_\gamma Q_{\beta\gamma}, \tag{29}$$

while $Q_{\beta\gamma}$ are given by:

$$Q_{ss} = \left| \frac{(n^2-1)\cos\phi_s}{\left(\cos\theta_i + \sqrt{n^2-\sin^2\theta_i}\right)\left(\cos\theta_s + \sqrt{n^2-\sin^2\theta_s}\right)} \right|^2, \tag{30}$$

$$Q_{sp} = \left| \frac{(n^2-1)\sqrt{n^2-\sin^2\theta_s}\sin\phi_s}{\left(\cos\theta_i + \sqrt{n^2-\sin^2\theta_i}\right)\left(n^2\cos\theta_s + \sqrt{n^2-\sin^2\theta_s}\right)} \right|^2, \tag{31}$$

$$Q_{ps} = \left| \frac{(n^2-1)\sqrt{n^2-\sin^2\theta_i}\sin\phi_s}{\left(n^2\cos\theta_i + \sqrt{n^2-\sin^2\theta_i}\right)\left(\cos\theta_s + \sqrt{n^2-\sin^2\theta_s}\right)} \right|^2, \tag{32}$$

$$Q_{pp} = \left| \frac{(n^2-1)\left(\sqrt{n^2-\sin^2\theta_i}\sqrt{n^2-\sin^2\theta_s}\cos\phi_s - n^2\sin\theta_s\sin\theta_i\right)}{\left(n^2\cos\theta_i + \sqrt{n^2-\sin^2\theta_i}\right)\left(n^2\cos\theta_s + \sqrt{n^2-\sin^2\theta_s}\right)} \right|^2 \tag{33}$$

Within the incidence plane $Q_{\beta\gamma} = 0$, while at a specular reflection direction $Q_{\beta\gamma} = R^2_\beta(\theta_i)$.

The fact that according to Rayleigh Rice model the BRDF scales with surface PSD has been widely exploited for optical characterization of the roughness in the case of slightly rough surfaces (which were generally understood as $\sigma << \lambda$). Meanwhile, the sample material also has an impact on the angular distribution of light scattered in reflection (through the reflectivity polarization factor Q). Moreover, the angular distribution of scattered light depends strongly on the polarization state of incident light (s, p).

As demonstrated in the 2000s by *Kawanishi et al.* first theoretically [13] and then experimentally [14], it is also possible to obtain zero-reflection at specific scattering angles for the p–polarized component of light scattered from rough surfaces. In analogy to classic Brewster effect, they referred to this scattering angle θ_r as the *Brewster scattering angle* θ^{sc}_B. In the case of scattering in reflection from a rough surface of the refractive index n in the air the Brewster scattering angle is as follows:

$$\sin\theta^{sc}_B = n\sqrt{\frac{n^2-\sin^2\theta_i}{n^2-\sin^2\theta_i+n^4\sin^2\theta_i}}. \tag{34}$$

This expression is a more compact form of the one provided by [14] and as a matter of fact was derived from Rayleigh-Rice formalism by setting $Q_{pp} = 0$ in eq.33. According to this expression, the dip in p–polarized light scattering does not depend on the surface

roughness and can appear at more than one angle of incidence.

Finally, at specular reflection from a surface with a Gaussian ACF the Rayleigh-Rice model reads as:

$$f_r\left(\theta_i, \pi, \theta_r = \theta_i, 0\right) = \frac{16\pi^3\sigma^2\ell_c^2}{\lambda^4}\cos^2\theta_i R^2(\theta_i). \tag{35}$$

According to this expression, the specular component of BRDF increases with the increase of surface roughness, which is both illogical and contradicting numerous experimental results.

Figure 14 shows the variation of BRDF at specular direction obtained from Kirchhof (a) and Rayleigh (b) models with s- and p-polarized illumination. Although the surface roughness will impact the amplitude of these curves, yet its the material properties - real and imaginary parts of refractive index which define their angle-dependance. For instance, the real part of refractive index defines the Brewster angle, while the imaginary part of refractive index impacts the shape of dip in the vicinity of Brewster angle. In non-absorbing media this dip is rather sharp, while even mild absorption decreases the depth of the dip around Brewster angle. This observations suggest that the specular component of BRDF measured under polarized illumination could be used for the estimation of both the refractive index of material and its surface property σ/ℓ_c^* (where ℓ_c^* is the correlation length of the surface with Gaussian ACF).

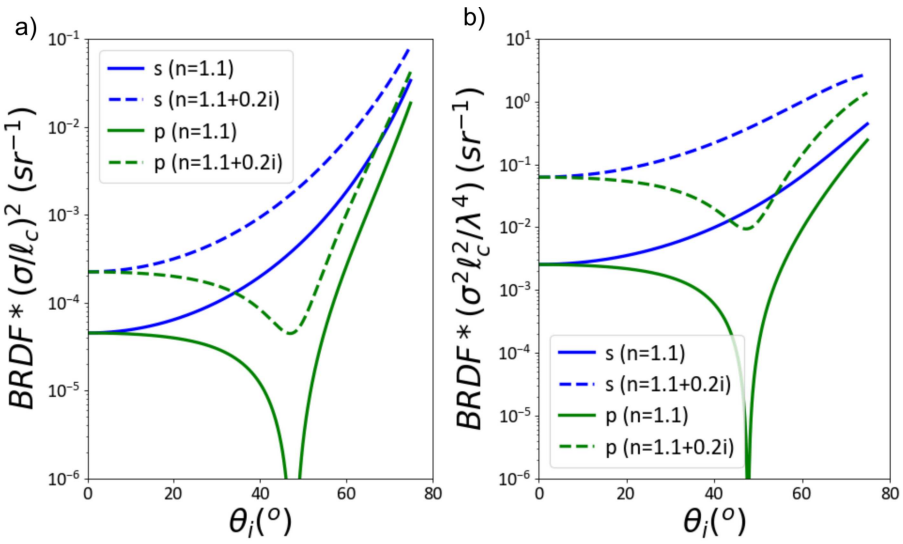

Figure 14. Variation of specular BRDF under s-polarized (blue curve) and p-polarized (green curve) illumination according to (a) Kirchhoff model (eq.25 for rough surface with Gaussian ACF) and (b) Rayleigh-Rice model (eq.35). Solid lines depict calculations for material with n=1.1, while dashed lines show results for slightly absorbing medium n=1.1+0.2i.

Note that the increase of specular BRDF with angle of incidence in Figure 14(b) is rather mild as compared to predictions by Kirchhoff model (see Figure 14(a)) and those expected for flat surfaces (see Figure 13(a)).
Thereby, in what follows we will analyze the amplitude of BRDF at specular reflection direction with Kirchhoff model, while the angular distribution of scattered light at given angle of incidence will be examined based on Rayleigh-Rice theory.

[1] J.C. Stover. *Optical scattering measurement and analysis,3rd edition.* SPIE, Bellingham, Washington USA, 2015.

[2] J.E. Harvey. *Understanding Surface Scatter: A Linear Systems Formulation,.* SPIE Press: Bellingham, United States, 2019.

[3] P. Beckmann and A. Spizzichino. *The scattering of electromagnetic waves from rough surfaces,.* Oxford: Pergamon Press, 1963.

[4] A. Soubret, G. Berginc, and C. Bourrely. Application of reduced rayleigh equations to electromagnetic wave scattering by two-dimensional randomly rough surfaces. *Phys. Rev. B*, 63:245411, 2001.

[5] R. L. Cook and K. E. Torrance. A reflectance model for computer graphics. *ACM Trans. Graph.*, 1:7–24, 1982.

[6] K. J. Dana, B. V. Ginneken, S. K. Nayar, and J. J. Koendrik. Reflectance and texture of real-world surfaces. *ACM Transact. on Graphics*, 18:1–34, 1999.

[7] E. P. F. Lafortune K. E. Torrance S. R. Marschner, S. H. Westin and D. P. Greenberg. Image-based brdf measurement including human skin,. *Eurographics Workshop on Rendering,Granada, Spain,June 21–23,*, 1999.

[8] M. Brand W. Matusik, H. Pfister and L. McMillan. A data-driven reflectance model,. *ACM Transactions on Graphics*, 22:759–769, 2003.

[9] E. R. Mendez A. G. Navarrete, E. I. Chaikina and T. A. Leskova. Experimental study of the reflectance of two-dimensional metal surfaces with a random roughness distribution. *J. Opt. Technol.*, 69:71–76, 2002.

[10] J.-J. Greffet S. Roux F. Plouraboue D. Vandembroucq, A. Tarrats. Light scattering from cold rolled aluminum surfaces. *Opt. Commun.*, 187:289–294, 2001.

[11] K.-O. Hauer A. Hope. Three-dimensional appearance characterization of diffuse standard reflection materials. *Metrologia*, 47:295–304, 2010.

[12] M. Born and E. Wolf. *Principles of Optics,7th ed.* Cambridge University Press, New York, 2012.

[13] H. Ogura T. Kawanishi and Z. L. Wang. Scattering of electromagnetic wave from a slightly random dielectric surfaceyoneda peak and brewster angle in incoherent scattering. *Waves Random Media*, 7:351 – 384, 1997.

[14] M. Kitano H. Ogura Z. L. Wang M. Izutsu T. Kawanishi, I. Iwata. Brewsters scattering angle and quasi-anomalous scattering in random scattering from dielectric interfaces. *J. Opt. Soc. Am. A*, 6:339–342, 1999.

[15] ISO 2813:2014. Paints and varnishes – determination of gloss value at 20 degrees, 60 degrees and 85 degrees, 2014.

[16] C. Turbil, J. Cabrero, I. Simonsen, D. Vandemroucq, and I. Gozhyk. Statistically representative estimators of multi-scale surface topography: example of aluminum blasted rough samples. *Surf. Topogr.: Metrol. Prop.*, 11:025018, 2023.

[17] Valtr M Necas D and Klapetek P. How levelling and scan line corrections ruin roughness measurement and how to prevent it. *Sci Rep*, 10:15294, 2020.

[18] Y. Zhao, G.-C. Wang, and T.-M. T.-M. Lu. *Experimental Methods in the Physical Sciences, Volume 37, Characterization of amorphous and crystalline rough surface principles and applications.* Academic Press, 2001.

[19] K. E. Torrance and E.M. Sparrow. Theory for off-specular reflection from roughened surfaces.

JOSA, 57:1105–1114, 1967.

[20] S. K. Nayar, K. Ikeuchi, and T. Kanade. Surface reflection: physical and geometrical perspectives. *IEEE Trans. Pattern Anal. Mach. Intell.*, 13:611–634, 1991.

[21] I. Simonsen J. Teisseire I. Gozhyk C. Turbil, T. S. HyukYoo and E. Garcia-Caurel. Experimental studies of the transmission of light through low coverage regular or random arrays of silica micropillars supported by a glass substrate. *Applied Optics*, 58:9267, 2019.

[22] ASTM D523-14. Standard test method for specular gloss,.

[23] R. S. Hunter. Methods of determining gloss. *Journal of Research of the National Bureau of Standards*, 18:19–42, 1937.

[24] R. S. Hunter and R. W. Harold. *The measurement of Appearance.* 2nd edition, 1987.

[25] M. Pelliccione and T.-M. Lu. *Evolution of thin film morphology.* Springer-Verlag, Berlin, Heidelberg, 2008.

[26] M. R. E. Lamont A. L. Gaeta M. Lipson K. Luke, Y. Okawachi. Broadband mid-infrared frequency comb generation in a si3n4 microresonator. *Opt. Lett.*, 40:4823–4826, 2015.

[27] P. B. Johnson and R. W. Christy. Optical constants of the noble metals. *Phys. Rev. B*, 6:4370–4379, 1972.

[28] T. M. Elfouhaily and C.-A. Guerin. A critical survey of approximate scattering wave theories from random rough surfaces. *Waves Random Media*, 14:R1R40, 2004.